



## A global benchmark of algorithms for segmenting the left atrium from late gadolinium-enhanced cardiac magnetic resonance imaging



Zhaohan Xiong<sup>a</sup>, Qing Xia<sup>b</sup>, Zhiqiang Hu<sup>c</sup>, Ning Huang<sup>d</sup>, Cheng Bian<sup>e</sup>, Yefeng Zheng<sup>e</sup>, Sulaiman Vesal<sup>f</sup>, Nishant Ravikumar<sup>f</sup>, Andreas Maier<sup>f</sup>, Xin Yang<sup>g</sup>, Pheng-Ann Heng<sup>g</sup>, Dong Ni<sup>h</sup>, Caizi Li<sup>i</sup>, Qianqian Tong<sup>i</sup>, Weixin Si<sup>j</sup>, Elodie Puybareau<sup>k</sup>, Younes Khoudli<sup>k</sup>, Thierry Géraud<sup>k</sup>, Chen Chen<sup>l</sup>, Wenjia Bai<sup>l</sup>, Daniel Rueckert<sup>l</sup>, Lingchao Xu<sup>m</sup>, Xiahai Zhuang<sup>n</sup>, Xinzhe Luo<sup>n</sup>, Shuman Jia<sup>o</sup>, Maxime Sermesant<sup>o</sup>, Yashu Liu<sup>p</sup>, Kuanquan Wang<sup>p</sup>, Davide Borra<sup>q</sup>, Alessandro Masci<sup>q</sup>, Cristiana Corsi<sup>q</sup>, Coen de Vente<sup>r</sup>, Mitko Veta<sup>r</sup>, Rashed Karim<sup>s</sup>, Chandrakanth Jayachandran Preetha<sup>t</sup>, Sandy Engelhardt<sup>u</sup>, Menyun Qiao<sup>v</sup>, Yuanyuan Wang<sup>v</sup>, Qian Tao<sup>w</sup>, Marta Nuñez-Garcia<sup>x</sup>, Oscar Camara<sup>x</sup>, Nicolo Savioli<sup>y</sup>, Pablo Lamata<sup>y</sup>, Jichao Zhao<sup>a,\*</sup>

<sup>a</sup> Auckland Bioengineering Institute, University of Auckland, Auckland, New Zealand

<sup>b</sup> State Key Lab of Virtual Reality Technology and Systems, Beihang University, Beijing, China

<sup>c</sup> School of Electronics Engineering and Computer Science, Peking University, Beijing, China

<sup>d</sup> SenseTime Inc, Shenzhen, China

<sup>e</sup> Tencent Jarvis Laboratory, Shenzhen, China

<sup>f</sup> Pattern Recognition Lab, Friedrich-Alexander-Universität Erlangen-Nürnberg, Erlangen, Germany

<sup>g</sup> Department of Computer Science and Engineering, The Chinese University of Hong Kong, Hong Kong

<sup>h</sup> National-Regional Key Technology Engineering Laboratory for Medical Ultrasound, School of Biomedical Engineering, Health Science Center, Shenzhen University, Shenzhen, China

<sup>i</sup> School of Computer Science, Wuhan University, Wuhan, China

<sup>j</sup> Shenzhen Key Laboratory of Virtual Reality and Human Interaction Technology, Shenzhen Institutes of Advanced Technology, Chinese Academy of Sciences, Shenzhen, China

<sup>k</sup> EPITA Research and Development Laboratory, Paris, France

<sup>l</sup> Department of Computing, Imperial College London, London, United Kingdom

<sup>m</sup> School of Naval Architecture, Ocean & Civil Engineering, Shanghai Jiao Tong University, Shanghai, China

<sup>n</sup> School of Data Science, Fudan University, Shanghai, China

<sup>o</sup> Inria, Université Côte d'Azur, Epione team, Sophia Antipolis, France

<sup>p</sup> School of Computer Science and Technology, Harbin Institute of Technology, Harbin, China

<sup>q</sup> Department of Electric, Electronic and Information Engineering, University of Bologna, Cesena, Italy

<sup>r</sup> Department of Biomedical Engineering, Eindhoven University of Technology, Eindhoven, the Netherlands

<sup>s</sup> School of Biomedical Engineering & Imaging Sciences, Kings College London, London, United Kingdom

<sup>t</sup> Faculty of Electrical Engineering and Information Technology, University of Magdeburg, Magdeburg, Germany

<sup>u</sup> Department of Internal Medicine III, Heidelberg University Hospital, Heidelberg, Germany

<sup>v</sup> Biomedical Engineering Center, Fudan University, Shanghai, China

<sup>w</sup> Department of Radiology, Leiden University Medical Center, Leiden, the Netherlands

<sup>x</sup> Physense, Department of Information and Communication Technologies, Universitat Pompeu Fabra, Barcelona, Spain

<sup>y</sup> Department of Bioengineering, Kings College London, London, United Kingdom

### ARTICLE INFO

#### Article history:

Received 14 April 2020

Revised 21 September 2020

Accepted 23 September 2020

Available online 16 October 2020

### ABSTRACT

Segmentation of medical images, particularly late gadolinium-enhanced magnetic resonance imaging (LGE-MRI) used for visualizing diseased atrial structures, is a crucial first step for ablation treatment of atrial fibrillation. However, direct segmentation of LGE-MRIs is challenging due to the varying intensities caused by contrast agents. Since most clinical studies have relied on manual, labor-intensive approaches, automatic methods are of high interest, particularly optimized machine learning approaches. To address

\* Corresponding author at: Auckland Bioengineering Institute, The University of Auckland, Private Bag 92019, Auckland 1142, New Zealand.

E-mail address: [j.zhao@auckland.ac.nz](mailto:j.zhao@auckland.ac.nz) (J. Zhao).

**Keywords:**  
 Left atrium  
 Convolutional neural networks  
 Late gadolinium-enhanced magnetic resonance imaging  
 Image segmentation

this, we organized the 2018 Left Atrium Segmentation Challenge using 154 3D LGE-MRIs, currently the world's largest atrial LGE-MRI dataset, and associated labels of the left atrium segmented by three medical experts, ultimately attracting the participation of 27 international teams. In this paper, extensive analysis of the submitted algorithms using technical and biological metrics was performed by undergoing subgroup analysis and conducting hyper-parameter analysis, offering an overall picture of the major design choices of convolutional neural networks (CNNs) and practical considerations for achieving state-of-the-art left atrium segmentation. Results show that the top method achieved a Dice score of 93.2% and a mean surface to surface distance of 0.7 mm, significantly outperforming prior state-of-the-art. Particularly, our analysis demonstrated that double sequentially used CNNs, in which a first CNN is used for automatic region-of-interest localization and a subsequent CNN is used for refined regional segmentation, achieved superior results than traditional methods and machine learning approaches containing single CNNs. This large-scale benchmarking study makes a significant step towards much-improved segmentation methods for atrial LGE-MRIs, and will serve as an important benchmark for evaluating and comparing the future works in the field. Furthermore, the findings from this study can potentially be extended to other imaging datasets and modalities, having an impact on the wider medical imaging community.

© 2020 Elsevier B.V. All rights reserved.

## 1. Introduction

### 1.1. Background

Segmentation is an important task for the quantitative analysis of medical images. In particular, delineation of a patient's internal organ and tissue structure from 3D computed tomography (CT) and magnetic resonance imaging (MRI) is often a necessity for medical diagnosis, patient stratification, and clinical treatment (Medrano-Gracia et al., 2015; Oakes et al., 2009; Csepe et al., 2017). Nowadays, various contrast agents are widely used to improve the visibility of disease-associated structures such as scarring, tumors, and blood vessels. For example, gadolinium-based contrast-enhancing agents are used in a third of all MRI scans (LGE-MRIs) worldwide and are proved to be very effective in providing clinical diagnosis of cardiac diseases (Oakes et al., 2009; Higuchi et al., 2017; Hennig et al., 2017; Figueras i Ventura et al., 2018). However, direct segmentation and analysis of atrial LGE-MRIs remain challenging due to the varying intensities caused by the increased enhancement of fibrotic tissue and imaging artifacts, as well as the varying quality of imaging. Therefore, the current standard of image segmentation and 3D reconstruction from these images for medical use still relies heavily on labor-intensive manual or semiautomatic methods (Csepe et al., 2017; Oakes et al., 2009; Higuchi et al., 2017). For instance, researchers and clinicians at the University of Utah have utilized atrial LGE-MRIs for cardiac research in the past two decades based on their well-established, although time-consuming workflow to manually label the left atrium (LA) from LGE-MRIs acquired from patients with atrial fibrillation (McGann et al., 2014), the most common cardiac arrhythmia.

### 1.2. Related work

In recent years, many approaches have been proposed for performing automatic 3D segmentation of the LA and other cardiac structures from medical images, mostly for non-contrast imaging. A 2013 benchmarking study held in conjunction with Medical Image Computing and Computer Assisted Intervention (MICCAI) examined methods for automatically segmenting the LA from non-contrast MRIs and CTs ( $N=30$  each) (Tobon-Gomez et al., 2015). The study revealed that methods combining statistical or atlas-based models with region growing approaches performed the best for both image types among 9 participants. A more recent 2017 benchmarking study for segmentation of left and right ventricles (LV/RV) from non-enhanced MRIs showed that convolutional neural networks (CNNs) significantly outperformed traditional meth-

ods (Bernard et al., 2018). By analyzing algorithms from 10 participants, the study revealed that the popular U-Net CNN architecture (Ronneberger et al., 2015) which was specifically designed for medical image segmentation was particularly effective. The top U-Net implementation achieved a Dice score of 93.1% for the LV and 89.9% for the RV, with Hausdorff distances of 6.9 mm and 12.2 mm, respectively.

Contrary to non-enhanced images, contrast-enhanced MRIs/CTs have received significantly less attention in terms of researching methods of segmentation to aid clinical procedures. A 2016 study was conducted to investigate methods of LA wall segmentation from LGE-MRIs and contrast-enhanced CTs ( $N=10$  each) by analyzing the submitted algorithms from three groups (Karim et al., 2018). However, due to the limited number of submitted algorithms, the study was unable to draw any definitive conclusions in terms of algorithm development, particularly with the three methods achieving Dice scores of approximately 55%. Other studies on LGE-MRI segmentation also have limited efficacy as the methods proposed required manually initialized shape priors, such as in the studies by Veni et al. (2017) and Zhu et al. (2013) which achieved average surface to surface distances of 3.2 mm and 2.8 mm, respectively. Since clinical settings require error distances to be minimized below 1–2 mm due to the thin atrial wall (2–3 mm) (Zhao et al., 2017), the methods mentioned were still lacking in terms of precision. Tao et al. (2016) proposed a method to reduce the distance error within 1.5 mm by incorporating paired magnetic resonance angiography into the pipeline. Zhu et al. was the only study that reported a Dice score of 79%.

While LGE-MRI segmentation still heavily relies on traditional methods, recent advancements in CNNs have been made for image segmentation in general. VGGNet (Simonyan and Zisserman, 2014) has been widely used for developing fully convolutional networks (Long et al., 2015; Noh et al., 2015) for semantic segmentation due to its simplicity, and adaptations of superior architectures, such as ResNet and Inception (Szegedy et al., 2017), are currently the state-of-the-art in the field (Chen et al., 2018b). Recent studies have investigated the use of CNN architectures for LA segmentation built upon the basic U-Net structure. Multi-scale convolutions and attention units have been incorporated into U-Net to form content-aware networks which enhance the learning of discriminative features and abnormalities from the complex LA and pulmonary vein structure (Du et al., 2020; Yang et al., 2020). Incorporation of CNNs into traditional multi-atlas and graph-cut pipelines have been conducted to utilize the feature learning capabilities in deep learning and maintain the anatomical accuracy of the segmentation (Li et al., 2020). However, these studies were evaluated on smaller datasets with different numbers of test samples, making direct comparisons difficult.

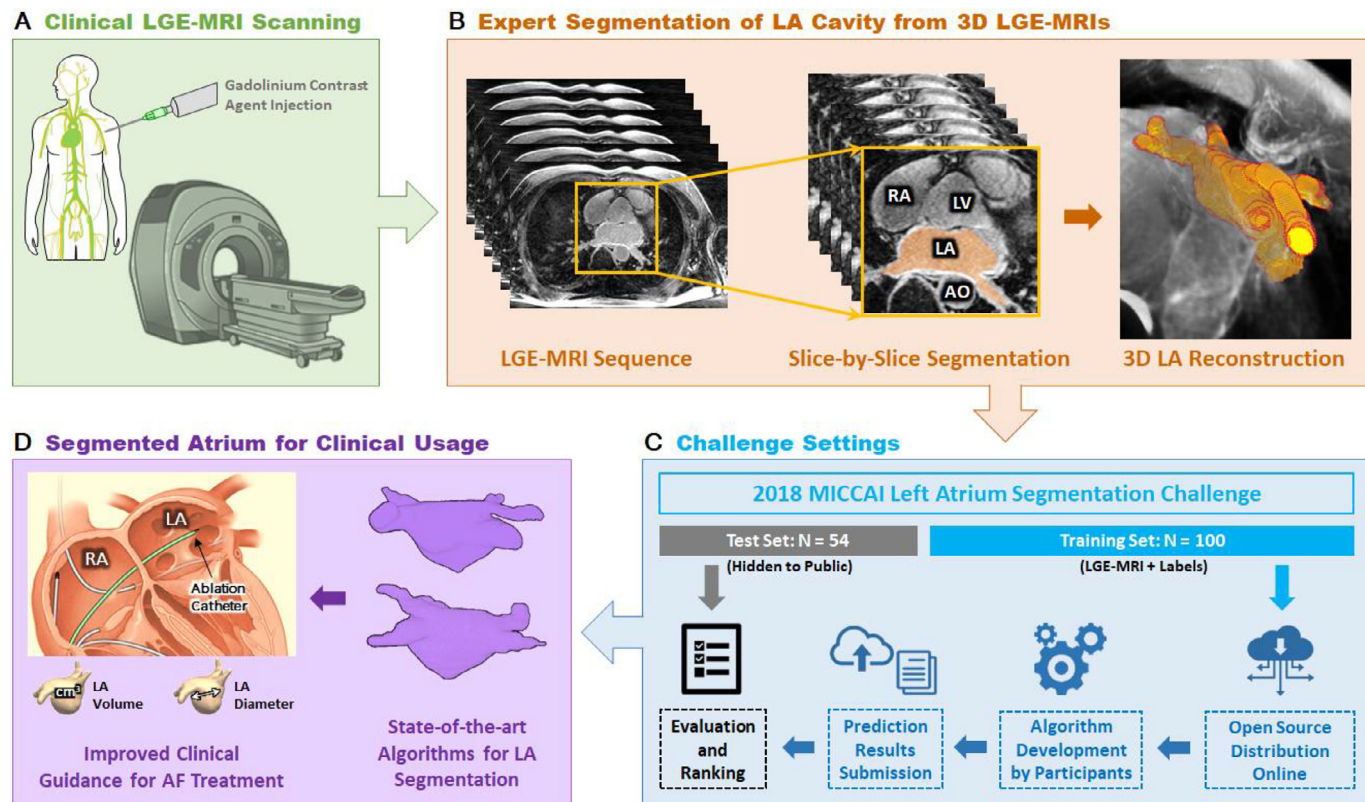


**Fig. 1.** The overall workflow of medical images for clinical usage and the 2018 Left Atrium (LA) Segmentation Challenge. **A)** Clinical MRI scanners were used to acquire late gadolinium-enhanced magnetic resonance imaging (LGE-MRIs) from patients with atrial fibrillation (AF). **B)** The LGE-MRIs were manually segmented in a slice-by-slice manner by experts to obtain labels of the LA cavity. The 3D LA geometry can be obtained by stacking the 2D segmentation together. **C)** In the 2018 LA Segmentation Challenge, 154 3D LGE-MRI data (each with a spatial dimension of either  $576 \times 576 \times 88$  or  $640 \times 640 \times 88$ ) were split into 100 training and 54 testing sets. The training data and labels were made public to all potential participants of the challenge, and the testing data was used at the end of the challenge for evaluation. A total of 27 teams participated and were ranked based on the Dice scores. **D)** Accurate reconstruction of the LA anatomical structure provides crucial information for patient stratification and for guiding clinical treatment for patients with AF. AO, aorta; LV, left ventricle; RA, right atrium.

### 1.3. Contribution

It remains unclear if it is possible to create a unified deep learning architecture capable of achieving optimal performance for segmentations across a wide spectrum of applications. While U-Net is currently the most widely used CNN architecture for medical image segmentation, and VGGNet and ResNet have been adapted as backbones and extended for segmentation in more recent developments, CNNs still have to be individually tuned for each specific application (Knoll et al., 2018; Zhu, 2019). This is reflected in the current literature which often contains wildly differing implementations of U-Net and other architectures for segmentation tasks in different disciplines, making it difficult to pinpoint design characteristics that can be applied universally. Methods for hyper-parameter optimization, particularly in U-Net, for general problems and/or specific tasks are still an ongoing topic of discussion, and could potentially lead to a more robust framework for segmentation. The lack of accessible, large-scale datasets and the varying quality of the image data (with labels) also hinders the development of optimized methods for LA segmentation from LGE-MRIs. By providing the largest 3D atrial LGE-MRI dataset along with top quality expert labelled LA cavities ( $N=154$ ) thanks to the great efforts of the University of Utah over the past two decades, we have gathered the community and organized the 2018 LA Segmentation Challenge (Fig. 1) in conjunction with the MICCAI conference and the Statistical Atlases and Computational Modelling of the Heart (STACOM) workshop in Granada, Spain (Pop et al., 2019). Throughout the course of the challenge, over 200 research

groups/individuals worldwide accessed our challenge dataset. In total, 27 teams participated in the final evaluation phase of the challenge and their final rankings are shown on the challenge website (<http://atriaseg2018.cardiacatlas.org/>).

To analyze the wide spectrum of conventional and deep learning methods submitted to the challenge, we first sub-grouped the methods by their main architecture designs and then identified the subgroup with the best design features which contributed to its superior performance. We then conducted extensive hyper-parameter tuning experiments on the top-performing method to identify the exact parameter choices leading to achieving state-of-the-art accuracies. By performing the benchmarking study in this manner, we offered both an overall picture on the major design choices necessary, as well as detailed practical considerations.

## 2. Methods and materials

### 2.1. Dataset and labels

A total of 154 independently acquired 3D LGE-MRIs from 60 de-identified patients with atrial fibrillation were used in this challenge. All patients underwent LGE-MRI scanning to define the atrial structure and fibrosis distribution prior to and post-ablation treatment at Utah (McGann et al., 2014; McGann et al., 2011). The clinical images were acquired with either a 1.5 Tesla Avanto or 3.0 Tesla Verio whole-body scanner (Siemens Medical Solutions, Erlangen, Germany). High-resolution LGE-MRIs of bi-atrial chambers were acquired approximately 20–25 min after the

injection of 0.1 mmol/kg gadolinium contrast (Multihance, Bracco Diagnostics Inc., Princeton, NJ) using a 3D respiratory navigated, inversion recovery prepared gradient echo pulse sequence. An inversion pulse was applied every heartbeat, and fat saturation was applied immediately before data acquisition. To preserve magnetization in the image volume, the navigator was acquired immediately after the data acquisition block. Typical scan times for the LGE-MRI study were between 8 and 15 min at 1.5 T and 6–11 min using the 3T scanner (for Siemens sequences) depending on patient respiration (McGann et al., 2014; McGann et al., 2011).

The spatial resolution of one 3D LGE-MRI scan was  $0.625 \times 0.625 \times 0.625 \text{ mm}^3$  with spatial dimensions of either  $576 \times 576 \times 88$  or  $640 \times 640 \times 88$  pixels. The LA cavity volumes were manually segmented in consensus and agreement with three trained observers for each LGE-MRI scan using the Corview image processing software to obtain one segmentation per scan (Merrk Inc, Salt Lake City, UT) (McGann et al., 2014) (Figure S1). The LA cavity was defined as the pixels contained within the LA endocardial surface including the mitral valve and LA appendage as well as the extent of the pulmonary vein (PV) sleeves. The endocardial surface border of the LA was segmented by manually tracing the LA and PV blood pool which were regions with enhanced pixel intensities in each slice of the LGE-MRI volume. The extent of the PV sleeves in the endocardial segmentation was limited to the PV antrum region and was defined as the point where the PVs stopped narrowing and remained constant in diameter. On average, the PV antra were limited to less than 10 mm extending out from the endocardial surface, or approximately three times the thickness of the LA wall. The LGE-MRI image volumes and associated LA segmentations were stored in the nearly-raw raster data (NRRD) format. The LGE-MRIs were grayscale and the segmentation labels were binary.

The dataset contained a range of imaging qualities, with the differences mostly being attributed to varying patient characteristics and magnetic fields. In order to explore the quality of the dataset, the signal to noise ratio (SNR), contrast ratio (CR), and heterogeneity (HET) between the foreground containing the LA and the background was assessed (Fig. 2A-C). The SNR, CR, and HET were defined as:

$$\text{SNR} = \frac{|\mu_{\text{LA}} - \mu_{\text{background}}|}{\sigma_{\text{background}}} \quad (1)$$

$$\text{CR} = \frac{\mu_{\text{LA}}}{\mu_{\text{background}}} \quad (2)$$

$$\text{HET} = \frac{\sigma_{\text{LA}}}{|\mu_{\text{LA}} - \mu_{\text{background}}|} \quad (3)$$

where  $\mu$  is the mean of either the LA pixels or background pixels of the LGE-MRI and  $\sigma$  is the standard deviation of either the LA pixels or background pixels of the LGE-MRI (Ulman et al., 2017). The three metrics used were in agreement as SNR had a strong positive correlation with CR and HET and while CR and HET had a strong negative correlation. Distributions of the quality measurements on all data showed that less than 15% of the data was of high quality ( $\text{SNR} > 3$ ), 70% of the data was of medium quality ( $\text{SNR} = 1$  to  $3$ ), and over 15% of the data was of low quality ( $\text{SNR} < 1$ ).

## 2.2. LA segmentation challenge

The 3D LGE-MRI dataset was randomly split into training ( $N=100$ ) and testing ( $N=54$ ) sets, with the entire training set published at the start of the challenge for participants to develop their algorithms. Images from the same patient were only in either the training or testing sets. The testing set was released without

the labels during the evaluation period near the end of the challenge, and participants were ranked based on the accuracy of the testing set predictions submitted to the organizers. The Dice score was used as the only evaluation metric in the challenge for simplicity. However, subsequent analyses with the surface to surface distance and the Euclidean distance error of the LA diameter and volume measurements were conducted after the challenge.

The 17 out of 27 teams who provided their methodologies and performances either in full STACOM papers (Xia et al., 2018; Bian et al., 2018; Vesal et al., 2018; Yang et al., 2018; Li et al., 2018; Puybareau et al., 2018; Chen et al., 2018a; Jia et al., 2018; Liu et al., 2018; Borra et al., 2018; de Vente et al., 2018; Preetha et al., 2018; Qiao et al., 2018; Nuñez-Garcia et al., 2018; Savioli et al., 2018) or Supplemental Materials (Huang, 2018; Xu et al., 2018) were included in this benchmarking study. Summaries of their methodologies are shown in Table 1 sorted by the final challenge rankings.

## 2.3. Algorithm evaluation

A range of metrics was used for the benchmarking study. Technical measures for evaluating participants included the Dice score, Intersection over Union (IoU) or Jaccard Index, sensitivity, specificity, Hausdorff distance (HD), and surface to surface distance (STSD). The Dice coefficient is the most commonly used metric for evaluating segmentation accuracy. Given a 3D prediction,  $A$ , and 3D ground truth,  $B$ , the Dice score is defined as

$$\text{DICE}(A, B) = \frac{2|A \cap B|}{|A| + |B|}. \quad (4)$$

The IoU (or Jaccard index) measures the similarity between a prediction and a ground truth and is defined as

$$\text{IoU}(A, B) = \frac{|A \cap B|}{|A \cup B|}. \quad (5)$$

Sensitivity and specificity are used to reflect the success of each algorithm for segmenting the foreground (LA cavity) and the background respectively

$$\text{Sensitivity} = \frac{TP}{TP + FN} \quad (6)$$

$$\text{Specificity} = \frac{TN}{TN + FP} \quad (7)$$

where TP stands for true positive, TN stands for true negative, FP stands for false positive, and FN stands for false negative. The HD measures the maximum local distance between the surfaces of the predicted LA volume and the ground truth. This metric evaluates geometrical characteristics, unlike the Dice or IoU which purely evaluates pixel-by-pixel comparisons. The 3D version of the HD was used in this study to measure the largest error distance of the 3D segmentation defined for a prediction of LA volume,  $A$ , and ground truth,  $B$ , as

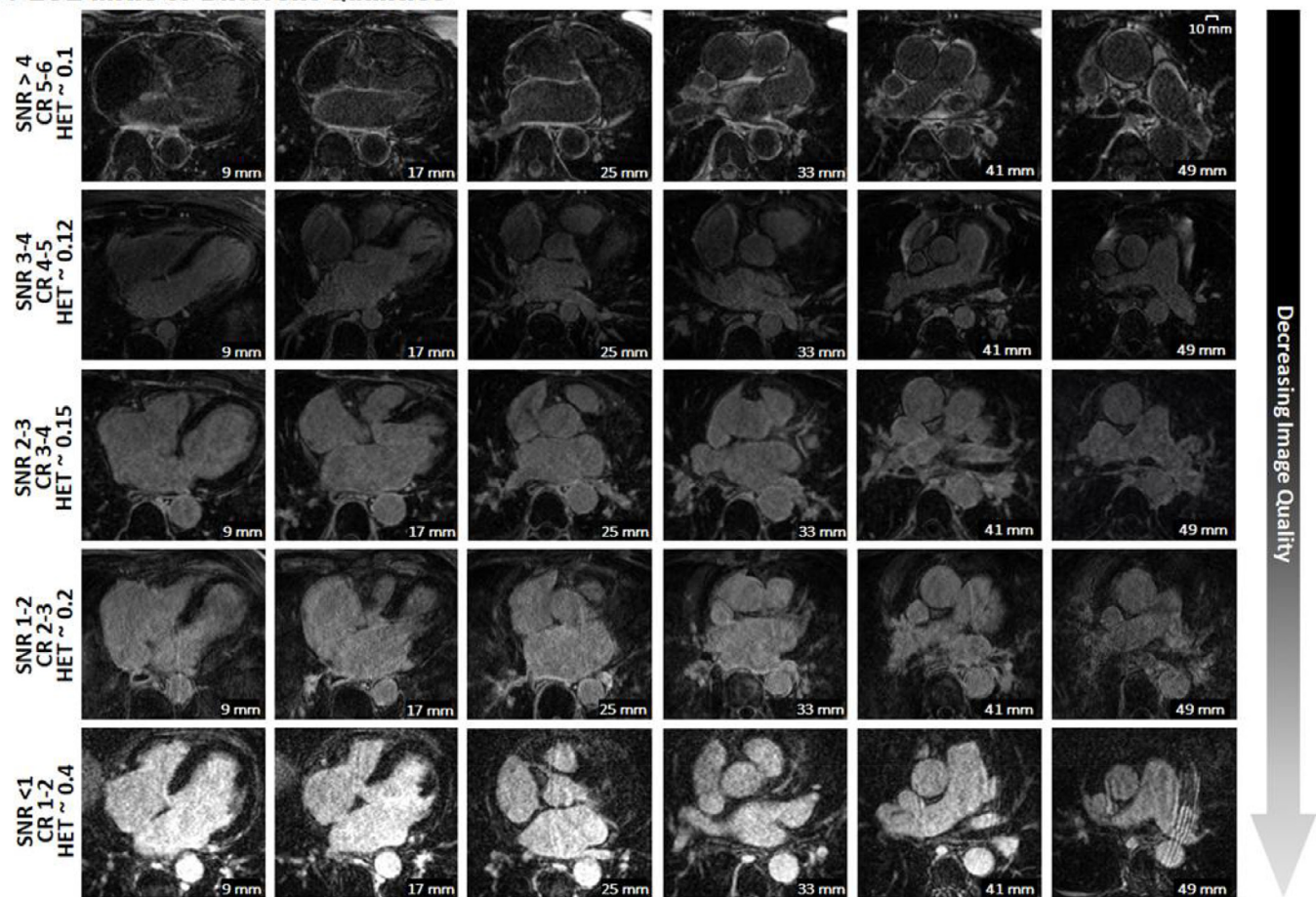
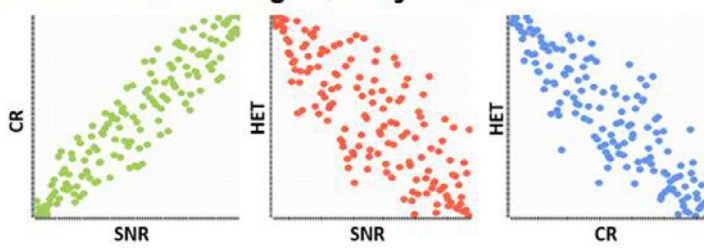
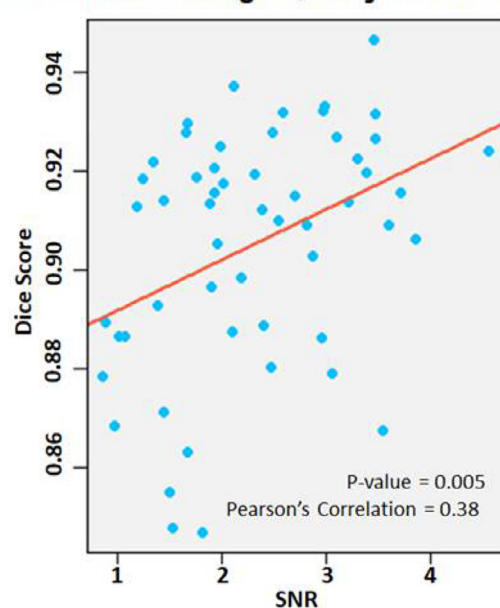
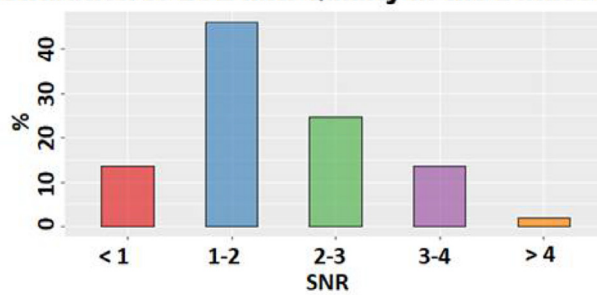
$$\text{HD}(A, B) = \max_{b \in B} \left\{ \min_{a \in A} \left\{ \sqrt{a^2 - b^2} \right\} \right\} \quad (8)$$

where  $a$  and  $b$  are all pixels locations within  $A$  and  $B$ . Lastly, the STSD measures the average distance error between the surfaces of the predicted LA volume and the ground truth as

$$\text{STSD}(A, B) = \frac{1}{n_A + n_B} \left( \sum_{p=1}^{n_A} \sqrt{p^2 - B^2} + \sum_{p'=1}^{n_B} \sqrt{p'^2 - A^2} \right) \quad (9)$$

where  $n_A$  is the number of pixels in  $A$ ,  $n_B$  is the number of pixels in  $B$ , and  $p$  and  $p'$  describe all points in  $A$  and  $B$ .

Biological measures for evaluating performance included the error of the LA anterior-posterior diameter and the error of the 3D

**A LGE-MRIs of Different Qualities****B Correlation of Image Quality Metrics****D Correlation of Image Quality vs Dice Score****C Distribution of LGE-MRI Quality in the Dataset**

**Fig. 2.** Variation in the quality of the late gadolinium-enhanced magnetic imaging (LGE-MRI) dataset used for this study. **A)** Each row represents different LGE-MRIs with various quality measured using signal to noise ratio (SNR), contrast ratio (CR), and heterogeneity (HET). The data at the top row has the highest quality and the data at the bottom row has the lowest quality. Each column represents 2D LGE-MRI at the same location within a 3D LGE-MRI and is shown with the distance measurements in millimeters. **B)** SNR and CR are positively correlated and are both negatively correlated with HET. **C)** Distribution of the SNR for all the 154 3D LGE-MRI datasets used in the 2018 Left Atrium Segmentation Challenge. **D)** Correlation of the average performance in relation to the LGE-MRI image quality, demonstrating that higher qualities (higher SNR) result in higher Dice scores.

**Table 1**

Summary of methods submitted to the 2018 Left Atrium Segmentation Challenge.

#	Dice (%)	Author	Pre-Processing	2D/3D	CNNs	Methodology	Post-Processing	Framework
1	<b>93.2 ± 2.2</b>	Xia et al.	Down sampling, CLAHE	3D	2	U-Net with additional residual connections to locate ROI, same network to segment ROI	None	PyTorch
2	<b>93.1 ± 2.2</b>	*Huang et al.	Down sampling	3D	2	U-Net with additional residual connections, dense connections and dilated convolutions to locate ROI, same network to segment ROI	None	Tensorflow
3	<b>92.6 ± 2.2</b>	Bian et al.	Cropping	2D	1	Dilated ResNet with spatial pyramid pooling to segment images	None	PyTorch
4	<b>92.5 ± 2.7</b>	Vesal et al.	Cropping, CLAHE	3D	1	U-Net with dilated convolutions to segment cropped region	None	Keras
5	<b>92.5 ± 2.3</b>	Yang et al.	Down sampling, cropping	3D	2	Faster-RCNN to locate ROI, U-Net with dense deep supervision to segment the ROI	None	Tensorflow
6	<b>92.3 ± 2.9</b>	Li et al.	None	3D	2	U-Net to locate ROI, U-Net with attention units and hierarchical aggregation units with dilated convolutions to segment the ROI	None	Keras
7	<b>92.3 ± 2.3</b>	Puybareau et al.	Normalization, cropping	2D	1	Fully convolutional network with pre-trained VGG-Net weights and intermediate output maps to segment image	Keep largest component, smoothing	Keras
8	<b>92.1 ± 2.6</b>	Chen et al.	Intensity normalization	2D	1	Multi-task U-Net with an additional classification branch at the center containing spatial pyramid pooling to classify if data is pre or post ablation, training is done on coarse images first then full-sized images to improve feature learning	Dilation and erosion, largest component	PyTorch
9	<b>91.5 ± 2.6</b>	*Xu et al.	Resize image to multiple scales, cropping	2D	1	Ensemble of different variants of U-Net to segment images of different scales and average the results	None	Tensorflow
10	<b>90.7 ± 3.1</b>	Jia et al.	Normalization, resizing	3D	2	U-Net to locate ROI and generate distance maps, ensemble of U-Nets to segment ROI and distance maps	None	Keras
11	<b>90.3 ± 3.2</b>	Liu et al.	Cropping	2D	1	U-Net to segment cropped region	None	Keras
12	<b>89.8 ± 3.4</b>	Borra et al.	Cropping based on thresholding	3D	1	U-Net to segment cropped region	Keep largest component	Keras
13	<b>89.7 ± 3.5</b>	De Vente et al.	Cropping	2D	1	U-Net to segment patches which were then stitched together to reconstruct the original image	Keep largest component	Keras
14	<b>88.7 ± 3.1</b>	Preetha et al.	Cropping	2D	1	U-Net with deep supervision to segment images	None	Tensorflow
15	<b>86.1 ± 3.6</b>	Qiao et al.	None	-	-	Convert image to probability map, atlas selection, multi-atlas registration, level-set refinement.	None	Non-Deep Learning
16	<b>85.9 ± 6.1</b>	Nuñez-Garcia et al.	None	-	-	Multi-atlas segmentation, shape modeling, clustering to rank similarity of different atria shapes	None	Non-Deep Learning
17	<b>85.1 ± 5.1</b>	Savioli et al.	Cropping, CLAHE, de-noise filters	3D	1	Fully convolutional network to segment entire image volume	None	Torch

CLAHE, contrast limited adaptive histogram equalization; CNN, convolutional neural network; ROI, region of interest.

LA volume between prediction and ground truth since LA diameter and volume are the two widely used clinical measures during the clinical diagnosis and treatment of patients with atrial fibrillation. The LA diameter, measured in millimeters, is calculated by finding the maximum Euclidean distance along the x-axis of each MRI scan to estimate the distance from the anterior LA to the posterior. The LA volume, measured in cm<sup>3</sup>, is calculated by summing the total number of positive (LA cavity) voxels.

Throughout the study, statistical significance was assessed using the two-tailed unpaired *t*-test to compare the performances of participant sub-groups as well as individual algorithms during analyses. Statistical comparisons between multiple groups were conducted using the Tukey honest significant differences (HSD) to perform multiple pairwise comparisons.

### 3. Results

#### 3.1. Performance of submitted algorithms

We first examined the overall performance of the different methodology categories from the 17 submitted algorithms. CNN was the most popular choice as it was used by 15 teams, and on average, substantially outperformed the other two teams which used traditional atlas-based segmentation methods (92.5% vs 85.1% Dice score,  $p < 0.05$ , Fig. 3A). Out of the 15 teams using CNNs, 12 teams proposed CNNs designs based on the popular U-Net architecture (Ronneberger et al., 2015) whilst the other three 3 implemented non-U-Net designs. We observed that the teams using U-Net based CNNs had superior performances (92.4% vs 89.3% Dice

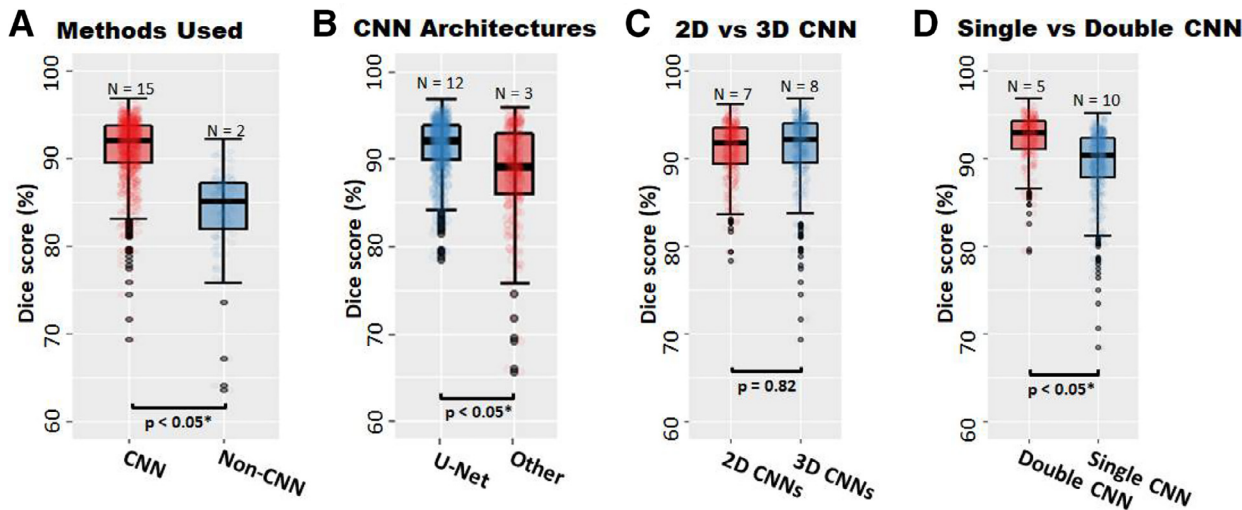


**Fig. 3.** Comparative summaries of the 17 algorithms included in this benchmarking study, a well representative subset of the 27 teams that participated in the 2018 Atrial Segmentation Challenge. **A)** The 15 methods utilizing convolutional neural networks (CNNs) outperformed the two traditional multi-atlas based methods with statistical significance. **B)** The 12 teams using U-Net architectures in their CNN pipelines outperformed the 3 teams using ResNet, VGGNet, and Fully-CNNs with statistical significance. **C)** Approximately an equal number of teams used methods consisting of 2D CNNs compared to methods consisting of 3D CNNs. However, there was no statistically significant difference in segmentation accuracy between the two groups. **D)** Participants using double, sequentially used CNNs achieved significantly higher accuracy than those using a single CNN for segmentation.

score,  $p < 0.05$ ) including Xia et al. (2018) and Huang (2018) who were ranked 1st and 2nd in the challenge (Fig. 3B). The majority of teams using the U-Net architecture implemented further enhancements to the original architecture in an attempt to improve the segmentation performance. This involved the use of additional residual connections (Xia et al., 2018), replacing all layers with dilated convolutions (Vesal et al., 2018), improved methods of training such as the use of custom loss functions, deep supervision (Yang et al., 2018), multi-task learning (Chen et al., 2018a), and attention mechanisms throughout the network (Li et al., 2018). The three teams which did not use U-Net as a baseline approach implemented enhanced versions of existing architectures such as ResNet (Bian et al., 2018; Szegedy et al., 2017), VGGNet (Simonyan and Zisserman, 2014; Puybareau et al., 2018), and Fully-CNNs (Long et al., 2015; Savioli et al., 2018; Xiong et al., 2019) which have been widely used on the ImageNet database (Deng et al., 2009). The Adam optimizer with a learning rate of 0.001 or 0.0001 was the most popular optimization configuration ( $N=12$ ), while the remaining teams used the stochastic gradient descent with a learning rate of 0.001, 0.0001 or 0.0005 ( $N=3$ ). The Adam optimizer with a learning rate of 0.001 was used by the top five teams and contributed to a significantly higher Dice score on average compared to teams which used a learning rate of 0.0001 and teams that used the stochastic gradient descent optimizer ( $p < 0.05$ ). There were no significant differences between the batch sizes used ( $p=0.5$ ). Investigation into the number of parameters in each proposed algorithm also showed no statistically significant correlation with the final challenge performance ( $p=0.21$ ) (Figure S2).

We then evaluated 2D versus 3D approaches based on the 15 submitted CNN algorithms. Since the challenge data was 3D, 8 out of the 15 teams proposed 3D CNNs which simply performed direct 3D segmentation on each set of 3D LGE-MRIs. On the other hand, 2D CNNs used by seven teams segmented each image slice of the image volume along the z-axis and stacked the individual segmentations together to obtain the final 3D results. Summary statistics show that there is no significant difference between the 2D and 3D CNN approaches when the CNN architecture and setup are not considered (92.1% vs 92.5% Dice score,  $p=0.82$ , Fig. 3C), even though the 3D CNNs were used by 4 of the top 5 teams. We also observed five teams utilizing a double, sequentially used CNNs in

their pipeline to improve the segmentation performance compared to methods that only contain a single CNN ( $N=10$ ). Through this enhancement, the former approach achieved a significantly better average Dice score of ~92.8% compared to single CNN methods which obtained a Dice score of ~90.3% on average ( $p < 0.05$ ) (Fig. 3D).

Of the methods discussed in our study, the *single CNN* method focused solely on using one CNN for direct segmentation of the LA from either the original dataset or ROIs cropped at a consistent location across all input images (Fig. 4A-B). Alternatively, the double, sequentially used CNNs, termed as *double CNN* throughout this study, involved the first CNN automatically detecting the region of interest (ROI) from LGE-MRIs and the second CNN performing regional segmentation of the LA from the ROIs (Fig. 4C). To further examine the 15 proposed CNN methodologies, we have regrouped the approaches into three categories: double 3D CNNs ( $N=5$ ), single 2D CNNs ( $N=7$ ), and single 3D CNNs ( $N=3$ ). It is noted that no team proposed a double 2D CNN method. The average accuracies of the three categories of CNN methods were evaluated with both technical and biological performance metrics: Double 3D CNN methods significantly outperformed single 2D and 3D CNN methods in terms of the Dice score (92.8% vs 91.1% and 89.9%,  $p < 0.05$ ), the surface to surface distance (0.75 mm vs 0.85 mm and 1.1 mm,  $p < 0.05$ ), LA diameter error (2.7% vs 3.2% and 4.3%,  $p < 0.05$ ), and LA volume error (4.5% vs 4.9% and 6.2%,  $p < 0.05$ ) (Fig. 4D-G). The success of the double CNN methodology can also be seen in the challenge rankings as this workflow was utilized by the top 2 teams as well as 4 of the top 6 teams which achieved over 92% Dice score.

### 3.2. Top performing CNN methodologies

Methods involving double 3D CNNs were shown to have the best overall performance, with illustrations of their architectures in Figures S3-S6. Interestingly, all five of the double 3D CNN methods adopted U-Net as the baseline architecture, though significant improvements were added to the baseline approach by these participants. These included the addition of residual connections into the U-Net by Xia et al. (2018) (Figure S3), Huang (2018) (Figure S4), and Li et al. (2018) (Figure S5). Specifically, residual connections

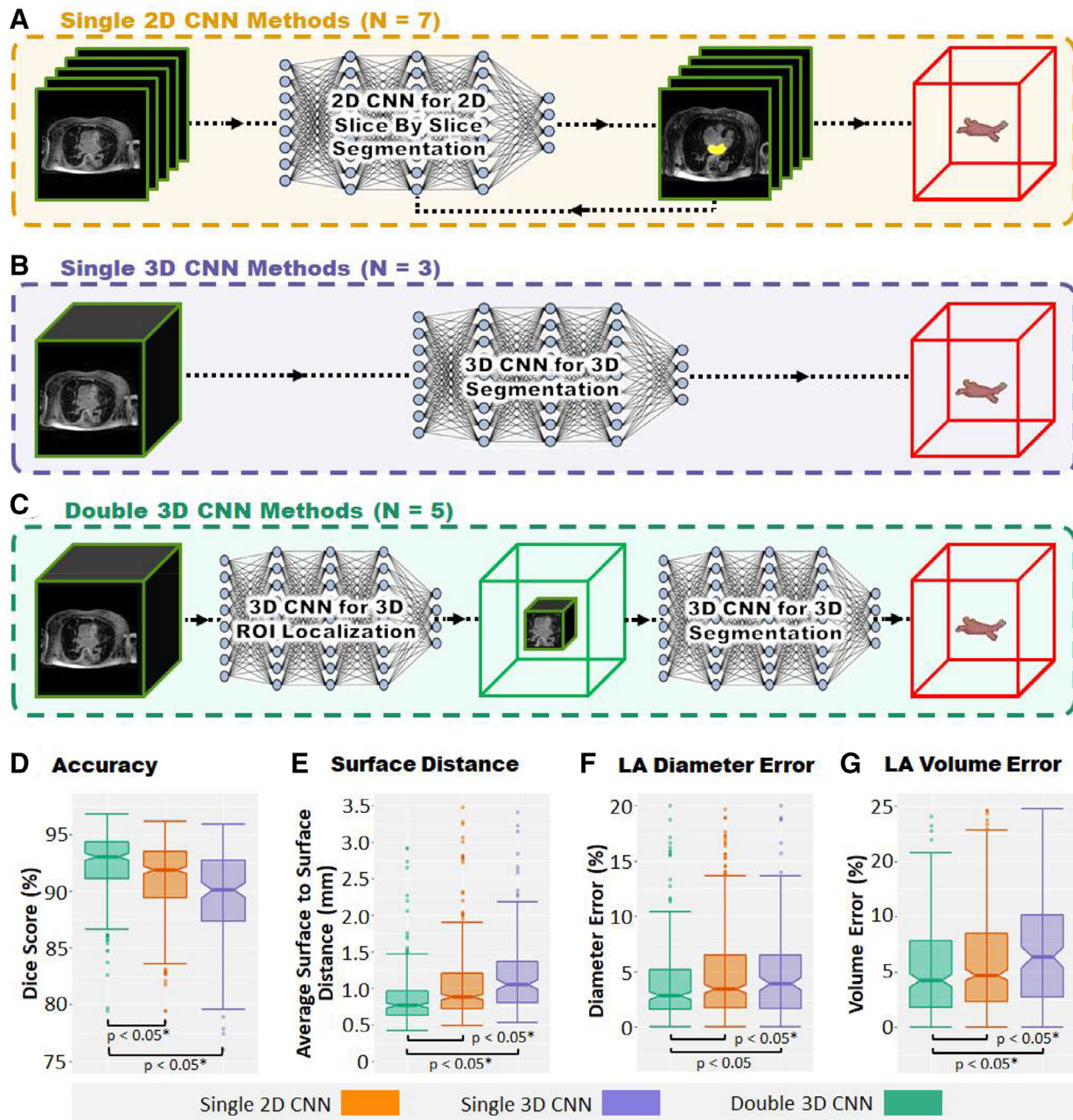


**Fig. 4.** Detailed evaluations of the performance of the 15 convolutional neural network (CNN) pipelines submitted to the challenge grouped into three general categories depending on how the CNNs were applied to segment the left atrium (LA) from the late gadolinium-enhanced magnetic resonance imaging (LGE-MRI). **A)** Single 2D CNN methods consisted of one 2D CNN which performed slice-by-slice segmentation of each LGE-MRI. The 3D LA was then reconstructed by stacking slice-by-slice segmentation. **B)** Single 3D CNN methods consisted of a single 3D CNN to segment the LA from the LGE-MRI volume directly. **C)** Double 3D CNN methods consisted of one CNN to detect a 3D region of interest (ROI) from the LGE-MRIs and a second CNN to segment LA from the 3D ROI. Dice score (**D**), the average surface to surface distance (**E**), LA diameter error (**F**) and LA volume error (**G**) comparisons showed the superiority of 3D double CNN methods among the three different categories of CNN workflows.

were added to each block of two to three sequential convolutional layers along the entire length of the networks to improve gradient flow during backpropagation when training the CNNs. The type of residual connections varied from a simple connection without any additional operations to more advanced connections containing convolutional and pooling layers. Dense connections were also seen in the method proposed by Huang (2018) along with dilated convolutions to improve the receptive field of the CNN. Yang et al. (2018) did not alter the U-Net architecture but instead elected for an improved dense supervision training scheme and a customized loss function (Figure S6). The proposed loss function was an en-

semble of the Dice score, pixel thresholding to improve sensitivity, and an overlap metric for improving segmentations at boundary locations. Apart from the double 3D CNN methods, Vesal et al. (2018) also performed highly with single 3D CNN methods. The effectiveness of their CNNs could be potentially attributed to the use of dilated convolutions, allowing them to outperform all other single CNN methods.

To gain further insights into the best performing CNN pipelines, control experiments were performed in this benchmarking study on the winning approach by Xia et al. (2018) to examine the factors contributing to their superior performance (Fig. 5). It

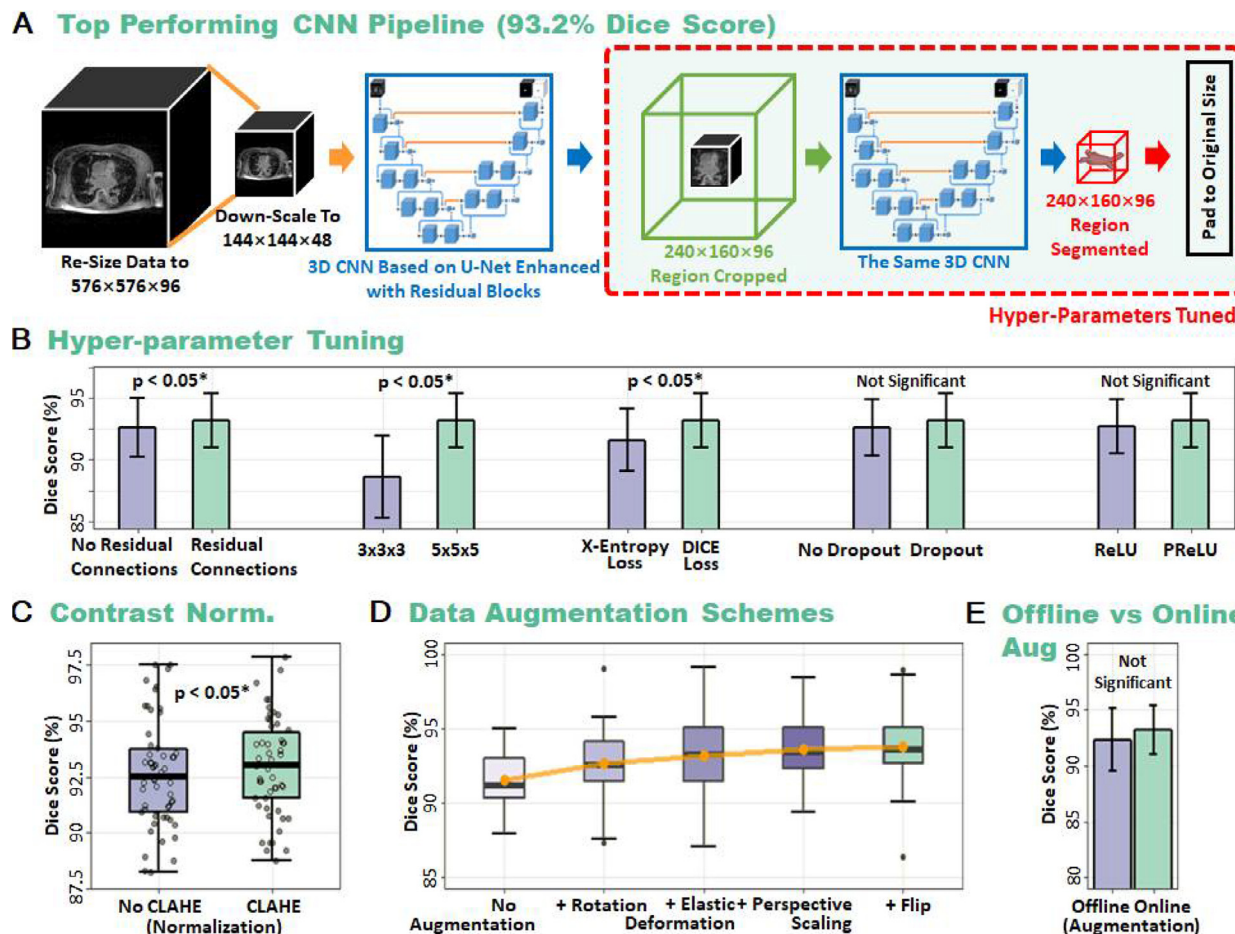


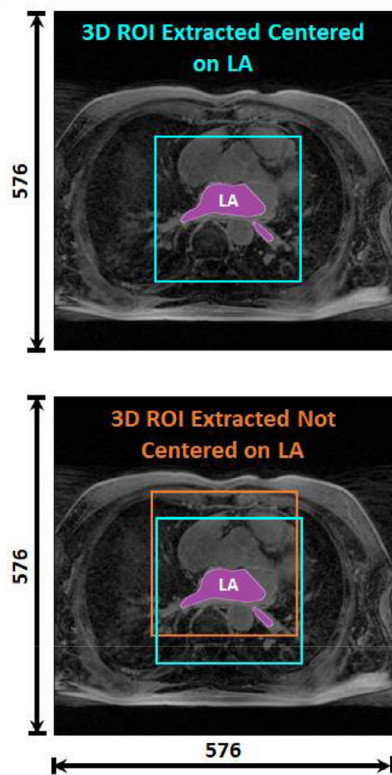
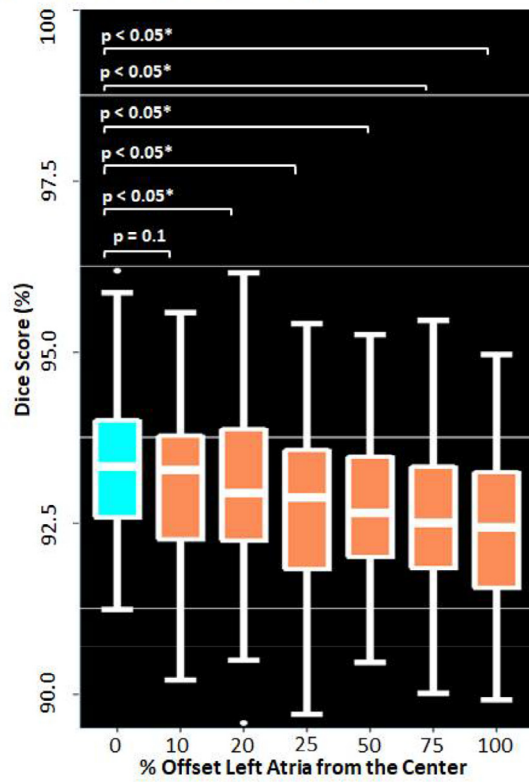
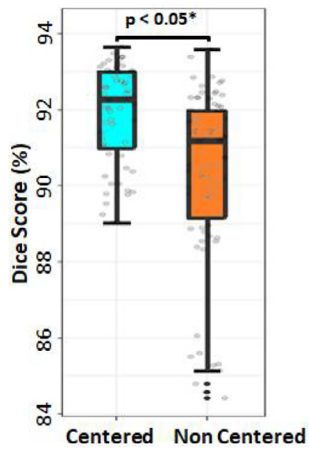
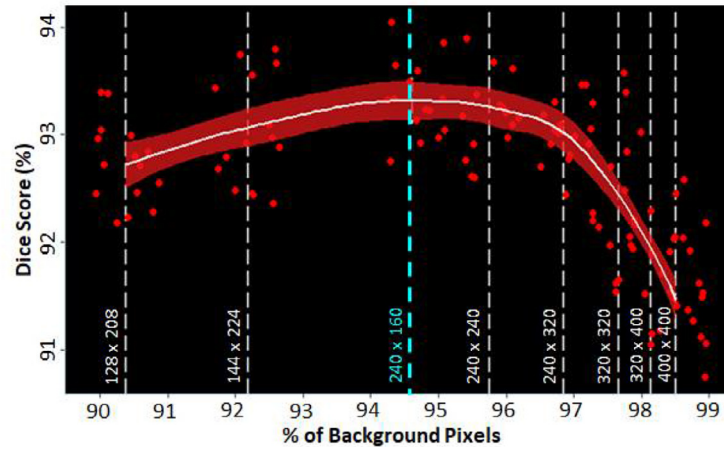
**Fig. 5.** Post-challenge analysis of the winning method by Xia et al. (2018) in the 2018 Left Atrium (LA) Segmentation Challenge demonstrates the optimality of their approach. **A)** Schematic summary of the 3D double convolutional neural network (CNN) approach. Both CNNs consisted of a U-Net architecture enhanced with batch-normalization in each layer and residual connections along the length of the network. The first CNN detected the centroid of the ROI from a down-sampled version of the initial late gadolinium-enhanced magnetic resonance imaging (LGE-MRI). A 240 × 160 × 96 region centered in the LA cavity was the output and was then processed by the second CNN to segment LA in 3D. The output was padded to obtain the original resolution of the input LGE-MRI. **B)** Hyper-parameter tuning of the U-Net architecture in the second CNN (red box) showed that all parameters used by the winning team were optimal through post-challenge analysis. **C)** The effect of contrast limited adaptive histogram equalization (CLAHE) for normalizing each LGE-MRI during pre-processing on the performance of the CNN. **D)** Data augmentation led to an incremental improvement as more augmentation methods were increasingly added, showing an increasing trend in accuracy. **E)** Comparisons of offline and online data augmentation schemes showing that there were no significant differences between the two schemes. (For interpretation of the references to colour in this figure legend, the reader is referred to the web version of this article.)

is noted that since most top-ranking algorithms utilized similar U-Net based designs, experimental observations derived from the approach by Xia et al. (2018) would also apply to other methods with similar algorithm setups. For the purposes of analysis, the top algorithm was selected based on its simplicity and light-weight nature. A summary of the participants' double 3D CNN pipeline is shown in Fig. 5A and additional experiments were conducted to evaluate the efficacy of the second CNN network for performing segmentation. Consistent with the benchmarking experiments, the algorithm was also trained using the 100 training data and tested using the 54 test data. Hyper-parameter tuning experiments in Fig. 5B revealed that the extra residual connections added to the U-Net architecture increased the Dice score by 0.7% ( $p < 0.05$ ). The increased receptive field using 5 × 5 × 5 convolutional kernels significantly improved the Dice score by 4% ( $p < 0.05$ ) compared to the widely used 3 × 3 × 3 kernels. The use of the Dice loss improved the accuracy by 2.1% ( $p < 0.05$ ) over the traditional cross-entropy loss which does not account for the major class imbalance present in the dataset. Although not statistically significant, dropout and parametric rectified linear unit (PReLU) further improved performance by approximately 0.5% ( $p = 0.1$  and  $p = 0.18$ ). Multi-variate statistical tests using all possible hyper-parameter combinations

were also performed (Figure S8), and the experiments yielded consistent results as in Fig. 5B. Color-intensity normalization or contrast limited adaptive histogram equalization (CLAHE), used by several teams improved the Dice score by 0.7% ( $p < 0.05$ ) (Fig. 5C). Standard data augmentation techniques such as random rotation, elastic deformations, perspective scaling, and random flipping improved the performance by over 2% ( $p < 0.05$ ) (Fig. 5D), while other schemes such as blurring, affine transformations, and shearing did not result in any significant improvements ( $p = 0.5$ ). We also observed that online augmentation, in which the images were augmented on-the-fly to produce differently augmented training sets during every epoch, was approximately similar to offline augmentation, in which an augmented set generated before training was used for all epochs ( $p = 0.41$ ) (Fig. 5E).

### 3.3. Key factors influencing the performance of double CNN approaches

We performed further analyses to target the key factors contributing to the success of double CNN methods compared to single CNNs. Since the optimality of the second CNN was shown through experimentation in the previous subsection, we

**A LA-Centered vs Offset****B Effect of Offsetting the LA****C Effect of Centering the LA on the ROIs****D Effect of CNN Input Size on Accuracy**

**Fig. 6.** Analysis of the key factors of the first convolutional neural network (CNN) in the double CNN methods in enhancing left atrium (LA) segmentation performance. **A)** Illustration of the region of interest (ROI) extracted from the double CNN methods centered on the LA (Top) and ROI extracted not centered on the LA (Bottom). The ROI not centered on the LA can be offset from the center of the LA by as much as 100 pixels in any direction (orange box). **B)** Displacing the LA by a distance in the ROI from the center of the patch reduced segmentation accuracy. A 100% offset implies the LA is pressed against the side of the patch without any loss of LA pixels. **C)** Performance summary comparing the methods proposed in the challenge which used double CNN pipelines to achieve an LA centered patch and the methods which had non-centered patches due to single CNN pipelines. **D)** To achieve the best accuracy, the size of the ROI should be sufficiently small. Effect of the input patch size of a CNN on the segmentation accuracy showing the peak accuracy at a patch size of 240 × 160 as proposed by the winners of the challenge. The percentage of background pixels is computed along the tested patch sizes to convey the degree of class imbalance in the CNN inputs where a higher percentage represents a more severe class imbalance. (For interpretation of the references to colour in this figure legend, the reader is referred to the web version of this article.)

focused on analyzing the key factors of the first CNN for influencing the final segmentation accuracy (Fig. 6). Firstly, it was observed that the ROI yielded as a result of the first CNN in a double CNN method was consistently centered on the LA (Fig. 6A). Without the ROI detection procedure undergone by the first CNN, the center of the LA would potentially have a ~100 pixel or ~17% shift in position from that of the original input images. Our exper-

iments show a decreasing trend in overall CNN performance as the LA (ROI) was purposely shifted away from the center of the image patch as an input for the second CNN, suggesting that centering the LA is extremely important to obtain superior accuracies (Fig. 6B and C). Secondly, we observed that the smaller the image patch of ROI as the output of the first CNN, the higher final segmentation accuracy. This relationship was true for all ROI sizes that were

Author	Dice (%)	IoU (%)	Sensitivity (%)	Specificity (%)	Hausdorff Distance (mm)	Surface to Surface Distance (mm)	P-Value	Number of Parameters
Xia et al.	93.2 (2.2)	87.4 (3.8)	93.6 (3.4)	99.952 (0.032)	8.892 (4.160)	0.748 (0.224)	0.23	21M
Huang et al.	93.1 (2.2)	87.2 (3.8)	93.7 (3.5)	99.949 (0.034)	8.495 (4.088)	0.754 (0.224)	0.29	2M
Bian et al.	92.6 (2.2)	86.9 (3.7)	93.3 (3.5)	99.951 (0.034)	9.213 (5.319)	0.759 (0.226)	0.32	45M
Yang et al.	92.5 (2.7)	86.1 (4.4)	94.3 (3.3)	99.932 (0.042)	9.759 (5.981)	0.850 (0.332)	0.98	3M
Vesal et al.	92.5 (2.3)	86.0 (3.9)	91.9 (4.5)	99.954 (0.029)	9.444 (4.671)	0.817 (0.240)	0.97	104M
Lee et al.	92.3 (2.9)	85.9 (4.9)	92.2 (5.2)	99.950 (0.030)	10.593 (7.109)	0.897 (0.442)	0.86	19M
Puybareau et al.	92.3 (2.3)	85.7 (3.9)	91.7 (4.1)	99.952 (0.030)	9.812 (5.676)	0.854 (0.252)	0.76	12M
Chen et al.	92.1 (2.6)	85.4 (4.3)	91.8 (4.3)	99.949 (0.034)	8.603 (4.710)	0.854 (0.245)	0.54	38M
Xu et al.	91.5 (2.6)	84.5 (4.3)	90.0 (3.9)	99.955 (0.025)	10.912 (5.000)	0.911 (0.258)	0.14	21M
Jia et al.	90.7 (3.1)	83.2 (5.1)	91.2 (5.4)	99.937 (0.038)	10.683 (5.976)	1.087 (0.496)	<0.05*	16M
Liu et al.	90.3 (3.2)	82.5 (5.2)	89.2 (4.8)	99.945 (0.037)	8.694 (3.841)	1.304 (0.845)	<0.05*	12M
Borra et al.	89.8 (3.4)	81.7 (5.4)	91.0 (6.9)	99.992 (0.034)	12.038 (5.586)	1.155 (0.454)	<0.05*	5M
De Vente et al.	89.7 (3.5)	81.5 (5.6)	88.9 (6.1)	99.938 (0.032)	9.766 (4.905)	1.132 (0.349)	<0.05*	28M
Preetha et al.	88.7 (3.1)	79.9 (4.9)	94.9 (3.0)	99.873 (0.048)	8.570 (3.486)	2.608 (1.933)	<0.05*	6M
Qiao et al.	86.1 (3.6)	75.8 (5.4)	84.7 (6.0)	99.923 (0.041)	11.834 (4.510)	1.449 (0.404)	<0.05*	-
Nuñez-Garcia et al.	85.9 (6.1)	75.8 (8.7)	84.5 (9.1)	99.250 (0.039)	12.690 (5.159)	1.473 (0.599)	<0.05*	-
Savioli et al.	85.1 (5.1)	74.4 (7.4)	83.6 (8.7)	99.917 (0.048)	14.659 (6.789)	1.611 (0.645)	<0.05*	2M

**Fig. 7.** Summary of the rankings for all participants under different technical metrics, sorted in descending Dice scores. Metrics included the Dice score, Intersection over Union (IoU/Jaccard Index), sensitivity, specificity, Hausdorff distance (HD) and average surface to surface distance performance measures. The color intensities reflect the rankings of the teams such that darker colors represent teams with higher performances. P-values for the statistical significance of each team computed with the Tukey Honest Significant Differences (HSD) are shown in the second to last column, with statistically significant values marked with an asterisk (\*). The number of parameters for each model in millions (M) is shown in the last column. . (For interpretation of the references to colour in this figure legend, the reader is referred to the web version of this article.)

greater than  $240 \times 160$  (dashed cyan line in Fig. 6D). The decreased input size of ROIs generated from the first CNN of the double CNN methods reduced the class imbalance as there were significantly fewer background pixels present in the input images, resulting in better performances as seen in our experiments using input sizes with X/Y dimensions of  $240 \times 160$  to  $400 \times 400$ . However, our experimentation also showed that the Dice accuracy of the CNN decreased when the size of the ROI was less than  $240 \times 160$  even though the LA was fully contained within the ROI. We postulate that the observed decrease in performance could be attributed to the boundary of the LA being too close to the edge of the ROI inputted into the CNN. U-Net is known to perform poorly when segmenting boundary regions (Ronneberger et al., 2015).

#### 4. Discussion and conclusions

##### 4.1. Characteristics of top-performing CNNs for segmentation

The key findings of this study are multifold. First of all, our study found that CNN approaches, notably those based on the U-Net architecture achieved better performance compared to traditional atlas-based methods and other CNN architectures. Additional residual connections and improved methods of optimization, such as custom loss functions, resulted in higher performance. The use of larger  $5 \times 5$  also contributed to improved segmentations over the most common  $3 \times 3$  kernels, potentially due to the increased

receptive field causing the CNN to capture an increased amount of structural information. In addition, our post-challenge analysis also showed that data augmentation methods and color-intensity or contrast normalization enhanced feature learning improved accuracy. More interestingly, 2D and 3D CNN methods had comparable accuracies. In particular, we discovered that double sequentially used CNN architectures achieved superior segmentation results than a single CNN approach. The effectiveness of the double CNN methods relies on two key elements. Firstly, the first CNN automatically detects the location of the ROI resulting in the image patch extracted to be centered on the ROI and sufficiently small to include minimal background pixels. Secondly, the second CNN effectively performs detailed regional segmentation of the ROI from the extracted image patch.

##### 4.2. Comparison of evaluation metrics

3D double CNNs achieved the highest performance on average, regardless of the evaluation metric used (Fig. 4). Our results show significant improvements over prior studies for LA segmentation from LGE-MRIs in terms of the surface to surface distance by approaching an average error of  $\sim 0.7$  mm (1 pixel) (Fig. 7). The Dice scores achieved in our study are also significantly higher than prior studies for LGE-MRIs, and are comparable to the accuracies reported by the studies on non-contrast MRI for segmenting the LA and ventricles. The high level of agreement between the main

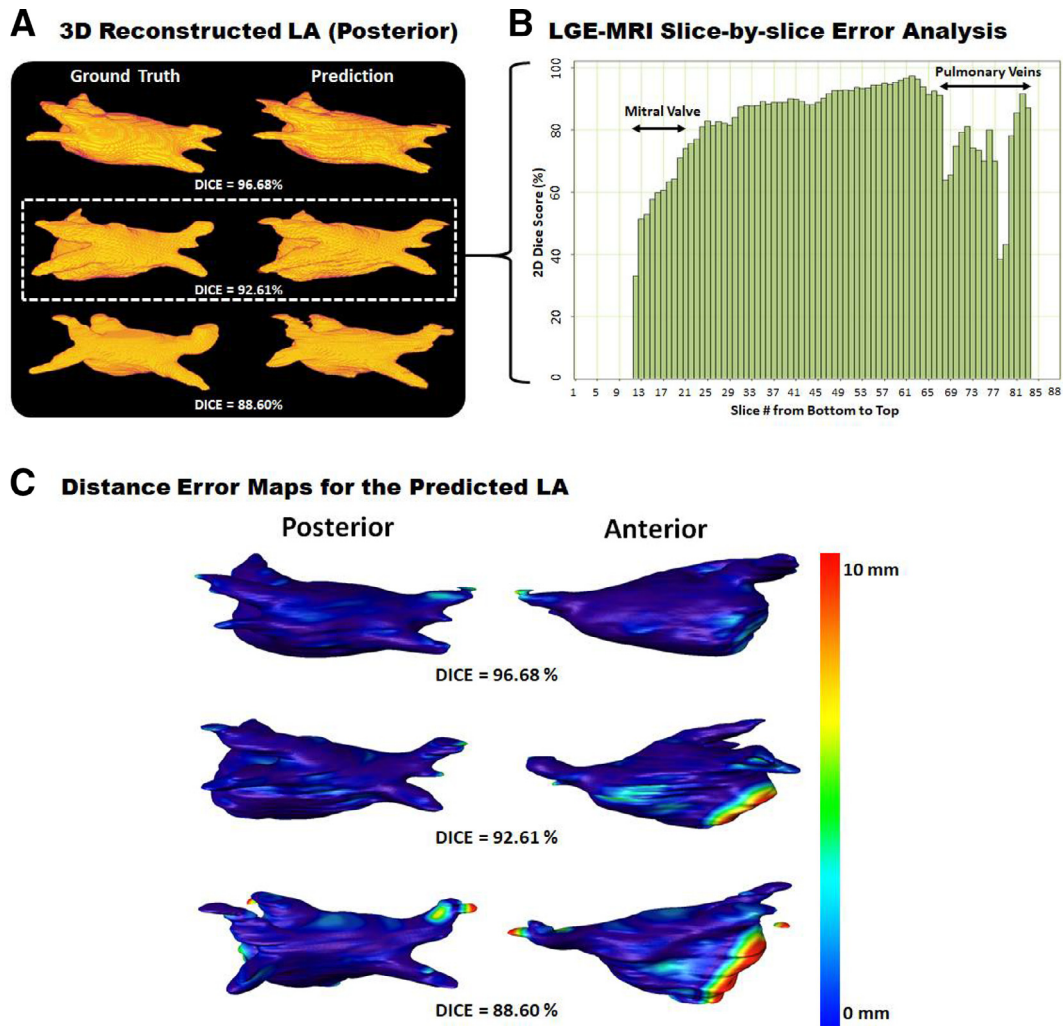


**Fig. 8.** Error analysis of predictions generated from the winning method by Xia et al. (2018) in the 2018 Left Atrium (LA) Segmentation Challenge. **A)** Visualization of predicted 3D LA reconstructions for three hearts with a high, medium, and low Dice scores. **B)** Slice-by-slice evaluation of the predicted LA reconstruction with a 3D Dice score of 92.61% in segmentation accuracy across each of the 88 slices in a 3D late gadolinium-enhanced magnetic resonance imaging (LGE-MRI). The most erroneous slices were at the bottom and top of the LA corresponding to the mitral valve and pulmonary veins, respectively. Slices 1 to 11 and 83 to 88 did not contain LA; hence, did not have any accuracy values. Note that the 2D Dice score used does not average out to the overall 3D Dice score due to the different dimensionality of the accuracy assessment. **C)** Surface to surface distance error maps of the segmented LA compared with the ground truth for the three hearts at the posterior (left) and anterior (right) views. The distance errors were normalized between 0 and 10 mm.

technical measures of Dice score and surface to surface distance and the biological measures of the LA diameter and volume error showed that the top-performing algorithms were capable of producing anatomically accurate segmentation, which is highly important in clinical applications. The most widely used segmentation metrics, the Dice score, Jaccard Index/IoU, and the surface to surface distance, produced fairly consistent rankings amongst the top 5 contestants (Fig. 7, Figure S9 and Figure S10). However, the Hausdorff distance, sensitivity, and specificity produced significantly different rankings in comparison. A potential explanation of this discrepancy is that the Hausdorff distance measured the most extreme errors, while sensitivity and specificity do not consider both positive and negative pixels simultaneously, leading to biased measurements. This also likely explains why these metrics are not commonly used for evaluating segmentation accuracies. While the conclusions drawn from the study based on the experimental results were validated with multiple technical and biological metrics, these summary results still suggest the ongoing need for an improved global definition of the exact meaning of high segmentation accuracy.

#### 4.3. Error analysis and future work

Error analysis of the top methods showed that although the 3D visualizations of the predicted LAs were similar to the ground truths, there are still potential improvements to be made. Slice-by-slice analysis of the predictions from the top team showed that the method performed poorly when segmenting the regions containing the PVs located at the superior slices of the 3D LGE-MRIs and the mitral valve at the bottom connecting the LA with the left ventricle (Fig. 8). The errors at the mitral valve were attributed to the fact that there are no clear landmarks to separate the two chambers. This leads the experts to label this region with a flat plane which potentially contains large variability, making it difficult to be reproduced by the CNNs. On the other hand, the errors at the PVs could be explained by the fact that these structures are often very small in size and vary greatly in shape among patients, making them difficult to detect. The inherently varying and relatively poor LGE-MRI qualities were also a factor which impacted the segmentation performance due to the low contrast of the images. Our analyses showed that the average accuracy for each LGE-MRI was

directly correlated to the quality of the particular LGE-MRI ratio for all approaches.

In the future, these issues could potentially be mitigated with an increased number of LGE-MRIs. Due to limitations with the current evaluation metrics, an interesting area to explore in future studies would be to create and design metrics computed through cardiologist assessments. To improve the optimization of CNN for specific tasks, the influence of the number of layers and kernels may be further investigated and tuned to increase performance. The concept of 2D double CNNs would also be another interesting direction for future research as it was not proposed by any of the teams, and may potentially be utilized to improve segmentation accuracies on more difficult tasks such as bi-atrial chamber segmentation.

#### 4.4. Conclusions

This study describes the 2018 LA segmentation challenge which provided 154 3D LGE-MRIs and analyses of the submitted algorithms. Our study found U-Net CNNs achieved the best performance, especially with the use of additional residual connections and advanced methods of optimization such as custom loss functions. Analysis also showed that 2D and 3D CNN methods had comparable accuracies. More interestingly, double sequentially used CNNs achieved superior segmentation results compared to single CNNs. Our extensive hyper-parameter tuning experiments also provide insights into the process of obtaining state-of-the-art accuracies. This large-scale benchmarking study makes a significant step towards much-improved segmentation methods for atrial LGE-MRIs, and will serve as an important benchmark for evaluating and comparing the future works in the field. We believe that findings from this study can potentially be extended to other imaging datasets and modalities, having an impact on the wider medical imaging community.

#### CRediT authorship contribution statement

Zhaohan Xiong: Data curation, Visualization, Investigation, Writing- Original draft preparation, Software, Validation. Qing Xia, Zhiqiang Hu, Ning Huang, Cheng Bian, Yefeng Zheng, Sulaiman Vesal, Nishant Ravikumar, Andreas Maier, Xin Yang, Pheng-Ann Heng, Dong Ni, Caizi Li, Qianqian Tong, Weixin Si, Elodie Puybareau, Younes Khoudli, Thierry Géraud, Chen, Wenjia Bai, Daniel Rueckert, Lingchao Xu, Xiahai Zhuang, Xinzie Luo, Shuman Jia, Maxime Sermesant, Yashu Liu, Kuanquan Wang, Davide Borra, Alessandro Masci, Cristiana Corsi, Coen de Vente, Mitko Veta, Rashed Karim, Chandrakanth Jayachandran Preetha, Sandy Engelhardt, Menyun Qiao, Yuanyuan Wang, Qian Tao, Marta Nuñez-Garcia, Oscar Camara, Nicolo Savioli and Pablo Lamata: Data curation, Writing - Original draft preparation and/or Writing- Reviewing and Editing. Jichao Zhao: Conceptualization, Supervision, Investigation and Writing - Reviewing and Editing.

#### Declaration of Competing Interest

The authors declare no conflict of interests.

#### Acknowledgements

The authors would like to thank Nvidia, MedTech CoRE New Zealand, and Arterys for providing prizes for the winners of the 2018 LA Segmentation Challenge. Z.X. and J.Z. are grateful for Nvidia for donating Titan-X Pascal GPU for algorithm development and testing, and the NIH/NIGMS Center for Integrative Biomedical Computing (CIBC) at the University of Utah for providing the LGE-MRI dataset. This work was funded by the [Health Research Council of New Zealand](#) [#16/385].

#### Supplementary materials

Supplementary material associated with this article can be found, in the online version, at [doi:10.1016/j.media.2020.101832](https://doi.org/10.1016/j.media.2020.101832).

#### References

- Bernard, O., Lalande, A., Zotti, C., Cervenansky, F., Yang, X., Heng, P.A., Cetin, I., Lekadir, K., Camara, O., Ballester, M.A.G., 2018. Deep learning techniques for automatic mri cardiac multi-structures segmentation and diagnosis: is the problem solved. *IEEE Trans. Med. Imaging* 37 (11), 2514–2525.
- Bian, C., Yang, X., Ma, J., Zheng, S., Liu, Y.A., Nezafat, R., Heng, P.A., Zheng, Y., 2018. Pyramid network with online hard example mining for accurate left atrium segmentation. In: *International Workshop on Statistical Atlases and Computational Models of the Heart*, pp. 237–245.
- Borra, D., Masci, A., Esposito, L., Andalò, A., Fabbri, C., Corsi, C., 2018. A semantic-wise convolutional neural network approach for 3-D left atrium segmentation from late gadolinium enhanced magnetic resonance imaging. In: *International Workshop on Statistical Atlases and Computational Models of the Heart*, pp. 329–338.
- Chen, C., Bai, W., Rueckert, D., 2018. Multi-task learning for left atrial segmentation on GE-MRI. In: *International Workshop on Statistical Atlases and Computational Models of the Heart*, pp. 292–301.
- Chen, L.C., Zhu, Y., Papandreou, G., Schroff, F., Adam, H., 2018. Encoder-decoder with atrous separable convolution for semantic image segmentation. In: *Proceedings of the European Conference on Computer Vision (ECCV)*, pp. 801–818.
- Csepe, T.A., Zhao, J., Sul, L.V., Wang, Y., Hansen, B.J., Li, N., Ignazzi, A.J., Bratasz, A., Powell, K.A., Kilic, A., 2017. Novel application of 3D contrast-enhanced CMR to define fibrotic structure of the human sinoatrial node *in vivo*. *Eur. Heart J.* 18 (8), 862–869.
- De Vente, C., Veta, M., Razeghi, O., Niederer, S., Pluim, J., Rhode, K., Karim, R., 2018. Convolutional neural networks for segmentation of the left atrium from gadolinium-enhancement MRI images. In: *International Workshop on Statistical Atlases and Computational Models of the Heart*, pp. 348–356.
- Deng, J., Dong, W., Socher, R., Li, L.J., Li, K., Fei-Fei, L., 2009. ImageNet: a large-scale hierarchical image database. In: *2009 IEEE Conference on Computer Vision and Pattern Recognition*, pp. 248–255.
- Du, X., Yin, S., Tang, R., Liu, Y., Song, Y., Zhang, Y., Liu, H., Li, S., 2020. Segmentation and visualization of left atrium through a unified deep learning framework. *Int J Comput Assist Radiol Surg* 1–12.
- Figueras i Ventura, R.M., Mărgulescu, A.D., Benito, E.M., Alarcon, F., Enomoto, N., Prat-Gonzalez, S., Perea, R.J., Borras, R., Chipa, F., Arbelo, E., 2018. Postprocedural LGE-CMR comparison of laser and radiofrequency ablation lesions after pulmonary vein isolation. *J. Cardiovasc. Electrophysiol.* 29 (8), 1065–1072.
- Hennig, A., Salel, M., Sacher, F., Camaiorni, C., Sridi, S., Denis, A., Montaudon, M., Laurent, F., Jais, P., Cochet, H., 2017. High-resolution three-dimensional late gadolinium-enhanced cardiac magnetic resonance imaging to identify the underlying substrate of ventricular arrhythmia. *Europace* 20, f179–f191.
- Higuchi, K., Cates, J., Gardner, G., Morris, A., Burgon, N.S., Akoum, N., Marrouche, N.F., 2017. The spatial distribution of late gadolinium enhancement of left atrial MRI in patients with atrial fibrillation. *JACC* 4 (1), 49–58.
- Huang, N., 2018. [https://www.dropbox.com/s/yyvij4352dax0q26/description\\_Ning\\_Huang.pdf?dl=0](https://www.dropbox.com/s/yyvij4352dax0q26/description_Ning_Huang.pdf?dl=0).
- Jia, S., Despinasse, A., Wang, Z., Delingette, H., Pennec, X., Jais, P., Cochet, H., Serment, M., 2018. Automatically segmenting the left atrium from cardiac images using successive 3D U-nets and a contour loss. In: *International Workshop on Statistical Atlases and Computational Models of the Heart*, pp. 221–229.
- Karim, R., Blake, L.E., Inoue, J., Tao, Q., Jia, S., Housden, R.J., Bhagirath, P., Duval, J.L., Varela, M., Behar, J., 2018. Algorithms for left atrial wall segmentation and thickness-evaluation on an open-source CT and MRI image database. *Med. Image Anal.* 50, 36–53.
- Knoll, F., Maier, A., Rueckert, D., 2018. Machine learning for medical image reconstruction: first international workshop. In: *MLMIR 2018*, Held in Conjunction with MICCAI 2018, Granada, Spain September 16, 2018 Proceedings.
- Li, L., Wu, F., Yang, G., Xu, L., Wong, T., Mohiaddin, R., Firmin, D., Keegan, J., Zhuang, X., 2020. Atrial scar quantification via multi-scale CNN in the graph-cuts framework. *Med Image Anal* 60, 101595.
- Li, C., Tong, Q., Liao, X., Si, W., Sun, Y., Wang, Q., Heng, P.A., 2018. Attention based hierarchical aggregation network for 3D left atrial segmentation. In: *International Workshop on Statistical Atlases and Computational Models of the Heart*, pp. 255–264.
- Liu, Y., Dai, Y., Yan, C., Wang, K., 2018. Deep learning based method for left atrial segmentation in GE-MRI. In: *International Workshop on Statistical Atlases and Computational Models of the Heart*, pp. 311–318.
- Long, J., Shelhamer, E., Darrell, T., 2015. Fully convolutional networks for semantic segmentation. In: *Proceedings of the IEEE Conference on Computer Vision and Pattern Recognition*, pp. 3431–3440.
- McGann, C., Akoum, N., Patel, A., Kholmovski, E., Revelo, P., Damal, K., Wilson, B., Cates, J., Harrison, A., Ranjan, R., 2014. Atrial fibrillation ablation outcome is predicted by left atrial remodeling on MRI. *Circulation* 7 (1), 23–30.
- McGann, C., Kholmovski, E., Blauer, J., Vijayakumar, S., Haslam, T., Cates, J., DiBella, E., Burgon, N., Wilson, B., Alexander, A., 2011. Dark regions of no-reflow on late gadolinium enhancement magnetic resonance imaging result in scar formation after atrial fibrillation ablation. *J. Am. Coll. Cardiol.* 58 (2), 177–185.

- Medrano-Gracia, P., Cowan, B.R., Suinesiaputra, A., Young, A.A., 2015. Challenges of cardiac image analysis in large-scale population-based studies. *Curr. Cardiol. Rep.* 17 (3), 9.
- Noh, H., Hong, S., Han, B., 2015. Learning deconvolution network for semantic segmentation. In: Proceedings of the IEEE International Conference on Computer Vision, pp. 1520–1528.
- Nuñez-Garcia, M., Zhuang, X., Sanroma, G., Li, L., Xu, L., Butakoff, C., Camara, O., 2018. Left atrial segmentation combining multi-atlas whole heart labeling and shape-based atlas selection. In: International Workshop on Statistical Atlases and Computational Models of the Heart, pp. 302–310.
- Oakes, R.S., Badger, T.J., Kholmovski, E.G., Akoum, N., Burgon, N.S., Fish, E.N., Blauer, J.J., Rao, S.N., DiBella, E.V., Segerson, N.M., 2009. Detection and quantification of left atrial structural remodeling with delayed-enhancement magnetic resonance imaging in patients with atrial fibrillation. *Circulation* 119 (13), 1758–1767.
- Pop, M., M. Sermesant, J. Zhao, S. Li, K. McLeod, A. Young, K. Rhode & K. Mansi. 2019. Statistical atlases and computational models of the heart. atrial segmentation and LV quantification challenges.
- Preetha, C.J., Haridasan, S., Abdi, V., Engelhardt, S., 2018. Segmentation of the left atrium from 3D gadolinium-enhanced MR images with convolutional neural networks. In: International Workshop on Statistical Atlases and Computational Models of the Heart, pp. 265–272.
- Puybareau, É., Zhao, Z., Khoudli, Y., Carlinet, E., Xu, Y., Lacotte, J., Géraud, T., 2018. Left atrial segmentation in a few seconds using fully convolutional network and transfer learning. In: International Workshop on Statistical Atlases and Computational Models of the Heart, pp. 339–347.
- Qiao, M., Wang, Y., van der Geest, R.J., Tao, Q., 2018. Fully automated left atrium cavity segmentation from 3D GE-MRI by multi-atlas selection and registration. In: International Workshop on Statistical Atlases and Computational Models of the Heart, pp. 230–236.
- Ronneberger, O., Fischer, P., Brox, T., 2015. U-net: convolutional networks for biomedical image segmentation. In: International Conference on Medical Image Computing and Computer-Assisted Intervention, pp. 234–241.
- Savioli, N., Montana, G., Lamata, P., 2018. V-FCNN: volumetric fully convolutional neural network for automatic atrial segmentation. In: International Workshop on Statistical Atlases and Computational Models of the Heart, pp. 273–281.
- Simonyan, K. & A. Zisserman. 2014. Very deep convolutional networks for large-scale image recognition. *arXiv preprint arXiv:1409.1556*
- Szegedy, C., Ioffe, S., Vanhoucke, V., Alemi, A.A., 2017. Inception-v4, inception-ResNet and the impact of residual connections on learning. In: Thirty-First AAAI Conference on Artificial Intelligence.
- Tao, Q., Ipek, E.G., Shahzad, R., Berendsen, F.F., Nazarian, S., van der Geest, R.J., 2016. Fully automatic segmentation of left atrium and pulmonary veins in late gadolinium-enhanced MRI: towards objective atrial scar assessment. *J. Mag. Reson. Imaging* 44 (2), 346–354.
- Tobon-Gomez, C., Geers, A.J., Peters, J., Weese, J., Pinto, K., Karim, R., Ammar, M., Daoudi, A., Margeta, J., Sandoval, Z., 2015. Benchmark for algorithms segmenting the left atrium from 3D CT and MRI datasets. *IEEE Trans. Med. Imaging* 34 (7), 1460–1473.
- Ulman, V., Maška, M., Magnusson, K.E., Ronneberger, O., Haubold, C., Harder, N., Matula, P., Matula, P., Svoboda, D., Radojevic, M., Smal, I., 2017. An objective comparison of cell-tracking algorithms. *Nat. Methods* 14 (12), 1141–1152.
- Veni, G., Elhabian, S.Y., Whitaker, R.T., 2017. ShapeCut: Bayesian surface estimation using shape-driven graph. *Med. Image Anal.* 40, 11–29.
- Vesal, S., Ravikumar, N., Maier, A., 2018. Dilated convolutions in neural networks for left atrial segmentation in 3D gadolinium enhanced-MRI. In: International Workshop on Statistical Atlases and Computational Models of the Heart, pp. 319–328.
- Xia, Q., Yao, Y., Hu, Z., Hao, A., 2018. Automatic 3D atrial segmentation from GE-MRIs using volumetric fully convolutional networks. In: International Workshop on Statistical Atlases and Computational Models of the Heart, pp. 211–220.
- Xiong, Z., Fedorov, V.V., Fu, X., Cheng, E., Macleod, R., Zhao, J., 2019. Fully automatic left atrium segmentation from late gadolinium enhanced magnetic resonance imaging using a dual fully convolutional neural network. *IEEE Trans. Med. Imaging* 38 (2), 515–524.
- Xu, L., X. Zhuang & X. Luo. 2018. [https://www.dropbox.com/s/e6n2gmjz88ugwi/description\\_Lingchao%C2%A0Xu.pdf?dl=0](https://www.dropbox.com/s/e6n2gmjz88ugwi/description_Lingchao%C2%A0Xu.pdf?dl=0).
- Yang, G., Chen, J., Gao, Z., Li, S., Ni, H., Angelini, E., Wong, T., Mohiaddin, R., Nyktari, E., Wage, R., Xu, L., 2020. Simultaneous left atrium anatomy and scar segmentations via deep learning in multiview information with attention. *Future Gener. Comput. Syst.* 107, 215–228.
- Yang, X., Wang, N., Wang, Y., Wang, X., Nezafat, R., Ni, D., Heng, P.A., 2018. Combating uncertainty with novel losses for automatic left atrium segmentation. In: International Workshop on Statistical Atlases and Computational Models of the Heart, pp. 246–254.
- Zhu, D., 2019. multimodal brain image analysis and mathematical foundations of computational anatomy. In: 4th International Workshop, MBIA 2019, and 7th International Workshop, MFCA 2019, Held in Conjunction with MICCAI 2019, Shenzhen, China October 17, 2019. Proceedings.
- Zhu, L., Gao, Y., Yezzi, A., Tannenbaum, A., 2013. Automatic segmentation of the left atrium from MR images via variational region growing with a moments-based shape prior. *IEEE Trans. Image Process.* 22, 5111–5122.
- Zhao, J., Hansen, B.J., Wang, Y., Csepe, T.A., Sul, L.V., Tang, A., Yuan, Y., Li, N., Bratasz, A., Powell, K.A., Kilic, A., 2017. Three-dimensional integrated functional, structural, and computational mapping to define the structural “fingerprints” of heart-specific atrial fibrillation drivers in human heart ex vivo. *J. Am. Heart. Assoc.* 6 (8), e005922.